

RESEARCH

Open Access



Pharmacokinetics modulation in solid tumors through thrombin-embedded nanomedicine

Sheng Lin^{1†}, Liuwei Zhang^{2†}, Hongyan Cui², Yue Wang^{3,4,5}, Yang Zheng^{5,6}, Jianhua Hu¹, Mingzhu Li^{5,7}, Wentao Wang^{3,4,5}, Shijia Zhang^{8,9}, Kehui Zhou^{8,9}, Qixian Chen^{2,5,10*}, Xiabin Lan^{8,9*} and Yan Zhao^{3,4,5*}

Abstract

The development of anti-tumor nanomedicines grapples with the critical challenge of achieving sustained retention and massive intratumoral distributions of chemotherapeutics. Herein, we attempted multifaceted prodrug nanomedicine with precise spatiotemporal responsiveness, integrating dual prodrugs—redox-responsive SN38 and pH-responsive thrombin and ensuring drug release coinciding with the striking tumor acidity and reductive stress, while its spatial selectivity is directed by the overexpression of integrins on cancerous cells. Most importantly, the thrombin component induces vascular occlusion within tumors, leading to normalization of the elevated interstitial fluid pressure and promoting accumulation of chemotherapeutic agents. This approach not only facilitates the massive intratumoral distribution of the nanomedicine but also ensures sustained retention of SN38 within the tumor microenvironment, thereby augmenting the cytotoxic potencies. Of note, the advanced mass spectrum mapping technology unprecedentedly validated the successful activation of the SN38 prodrug and massive distribution throughout the solid tumors for thrombin-containing nanomedicine, in stark to apparent entrapment in tumor vasculature and stroma for the conventional thrombin-free nanomedicine. Hence, the multifunctionalities of our proposed dual prodrug nanomedicine is underscored by its ability to actively target cancerous cells, induce vasculature occlusion, and orchestrate a controlled release of chemotherapeutic agents.

Keywords Solid tumor, Nanomedicine, Targeted drug delivery, Prodrug nanomedicine, Tumor microenvironment-responsive, Synergistic anticancer therapy

Introduction

The advent of anti-tumor nanomedicines marks a significant frontier in oncological therapeutics, heralding the potential to augment drug delivery, amplify therapeutic efficacy, and attenuate systemic toxicity [1–2]. Central to this endeavor is the imperative challenge of achieving sustained retention and extensive intratumoral distribution of chemotherapeutic agents within the intricate and heterogeneous tumor microenvironment (TME) [3, 4]. The non-uniform distribution of nanomedicines within neoplastic lesions has emerged as a pivotal barrier, impeding their clinical translation and therapeutic success [5–7].

[†]Sheng Lin and Liuwei Zhang contributed equally to this work.

*Correspondence:

Qixian Chen

plasmid@zju.edu.cn

Xiabin Lan

lanxb@zjcc.org.cn

Yan Zhao

zhaoyan@cancerhosp-ln-cmu.com

Full list of author information is available at the end of the article



Historically, the Enhanced Permeability and Retention (EPR) effect has underpinned nanomedicine design, predicated on the notion that the compromised vasculature of tumors would facilitate the passive targeting of nanocarriers to tumor sites [8]. However, contemporary evidence has contested this paradigm, elucidating that nanomedicine accumulation and distribution within tumors exhibit profound heterogeneity and variability, both inter- and intra-tumoral [3]. This heterogeneity is modulated by a multitude of determinants, encompassing tumor vascular architecture, stromal content, and microenvironment morphology.

The spatial distribution of nanomedicines is paramount for therapeutic efficacy, as it directly influences local drug concentrations and target engagement. Heterogeneous accumulation and distribution may precipitate variable efficacy across distinct tumor regions, ultimately compromising the overall therapeutic outcome. Previous studies have demonstrated that a minuscule fraction of systemically administered nanomedicines successfully reach the tumor sites [9], with a substantial portion being sequestered in extracellular domains, underscoring the imperative for strategies that enhance both intratumoral accumulation and penetration.

The temporal distribution of nanomedicines is equally critical, as it dictates the spatial distribution and precipitates the release of free drugs, which is essential for antitumor efficacy. The complex TME, characterized by a dense extracellular matrix, abundant stromal cells, and heterogeneous tumor cells, poses significant challenges to the effective targeting of tumor cells by nanomedicine [10].

In light of these challenges, there is a burgeoning consensus that a profound understanding of how tumor features influence nanomedicine accumulation, distribution, and retention is *sine qua non* for the design of more efficacious anti-cancer nanomedicinal therapeutics. High-resolution 3D visualization techniques have begun to elucidate the heterogeneity of nanomedicine distribution within solid tumors, revealing pronounced differences in distribution patterns influenced by vascular patterns, stromal contents, and microenvironment morphologies [7]. Thus, addressing the non-uniform distribution of nanomedicines within tumors is a multifaceted problem that necessitates a nuanced approach to nanomedicine design and evaluation. Conquering this challenge is essential for harnessing the potential of nanomedicine to improve clinical outcomes for patients with cancer.

In this context, our approach encompasses the innovative incorporation of thrombin, which is posited to modulate tumor angiogenesis by inducing thrombosis and impairing the formation and function of tumor vasculature. This strategy is anticipated to elicit vascular degeneration and ischemia within tumors, thereby inhibiting

tumor growth and metastasis. The therapeutic potential of thrombin starvation is further augmented by its ability to modulate endogenous factors such as tumor hypoxia and drug resistance, which are known to attenuate the efficacy of conventional chemotherapy.

Most importantly, this *avant-garde* approach is predicated on the induction of intra-tumoral vascular occlusion, which is posited to ameliorate elevated interstitial fluid pressure and thereby facilitate the pervasion of chemotherapeutic agents into the neoplastic mass. This strategy effectively mitigates their systemic recirculation and subsequent dilution, enhancing the cytotoxic milieu within the tumor and augmenting therapeutic outcomes. This *avant-garde* approach offers a novel and potentially transformative therapeutic intervention for this refractory oncological condition.

Results and discussion

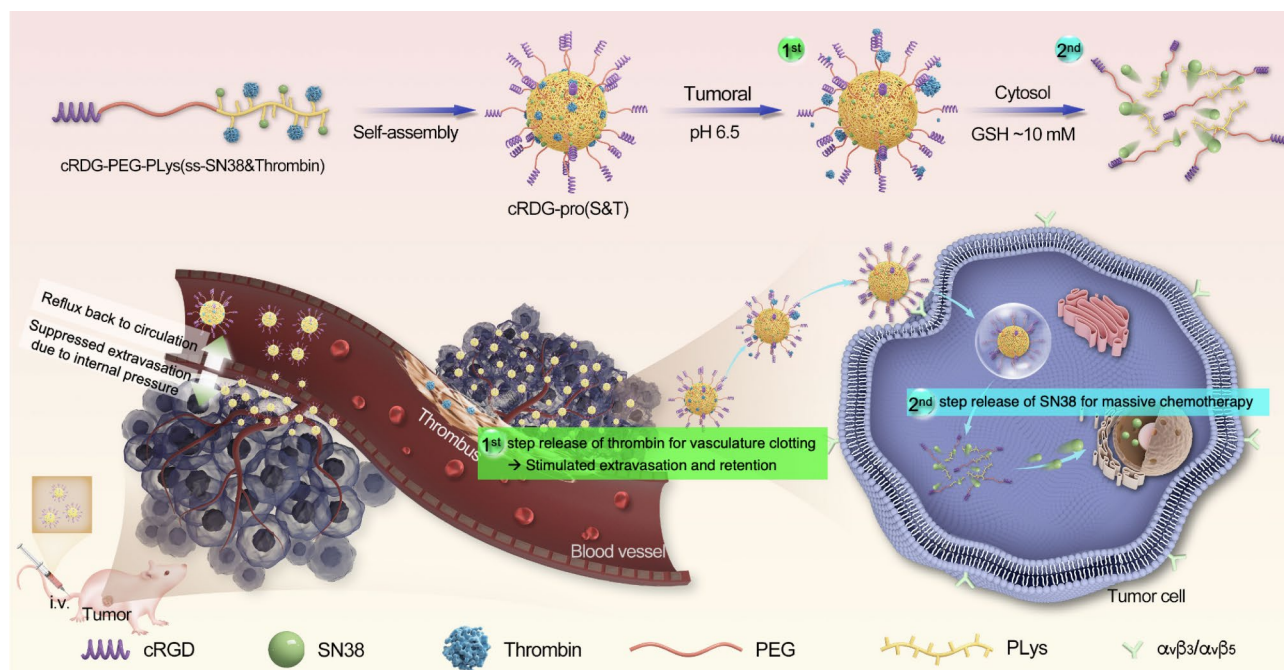
Triple-negative breast cancer (TNBC) represents a highly aggressive and heterogeneous neoplasm, which is notoriously refractory to monotherapy, partly attributable to the lack of expression of estrogen receptors, progesterone receptors, and human epidermal growth factor receptor 2 (HER2) overexpression [11–14]. This molecular profile confers a particularly poor prognosis. In the realm of chemotherapy, clinical efficacy is often compromised by the nonspecific distribution of chemotherapeutic agents and the resultant systemic toxicities. Therefore, there is a pressing need for the development of targeted drug delivery systems that can orchestrate the precise and temporally controlled delivery of chemotherapeutic agents to the tumor microenvironment. There is a burgeoning interest in the engineering of stimuli-responsive prodrugs that are selectively activated within the tumor microenvironment and the integration of combinatorial therapeutic strategies that leverage the synergistic effects of multiple treatment modalities [15–17].

The emergence of nanoplateform-based combinatorial therapeutics has heralded a paradigm shift in the management of TNBC [18, 19]. The utilization of nanoplateforms, capable of encapsulating a diverse array of therapeutic agents, offers a multitude of compelling advantages [20–24]. Notably, irinotecan (CPT-11), a synthetic analogue of the natural alkaloid camptothecin, exerts its anti-neoplastic effects by inhibiting topoisomerase I, thereby disrupting DNA replication and inducing apoptosis in tumor cells [20]. The principal active metabolite, 7-ethyl-10-hydroxycamptothecin (SN38), demonstrates significantly enhanced anti-tumor efficacy compared to CPT-11. The direct clinical application of SN38 bypasses the metabolic activation issues associated with CPT-11. However, its aqueous insolubility and challenges in pharmaceutical formulation present significant obstacles.

In our current investigations, we have strategically developed nanoscale drug delivery systems by incorporating the targeting moiety cyclic Arg-Gly-Asp (cRGD), hereinafter referred to as cRGD-poly(ethylene)-polylysine (cRGD-PEG-PLys). Concurrently, a comparative control group, devoid of the cRGD ligand, designated as PEG-PLys, was synthesized (refer to Fig. S3 in the Electronic Supplementary Information [ESI⁺]). The cytotoxic agent of SN38 was conjugated to the amphiphilic cRGD-PEG-PLys via redox-sensitive disulfide bonds, resulting in the formation of a novel class of amphiphilic compounds, denoted as [cRGD-PEG-PLys(ss-SN38): cRGD-pro(S)] (Fig. S4). To incorporate thrombin into the SN38-nanomedicine construct, thrombin underwent covalent carboxylation and was subsequently covalently linked to the lysine residues through maleic anhydride, thus endowing the system with responsiveness to the acidic conditions of the tumor microenvironment. These components self-assembled into micelles, which further coalesced into nanoparticles, designated as cRGD-pro(S&T) NPs. For comparative analysis, a spectrum of control groups was synthesized, including cRGD-pro(S) (thrombin-deficient), cRGD-pro(T) (SN38-deficient), pro(S) (deficient in cRGD and thrombin), pro(S&T) (deficient in cRGD), and others.

The cRGD-pro(S&T) NPs are engineered to actively engage with integrins that are aberrantly overexpressed on the surfaces of neoplastic cells. Upon exposure to the acidic condition's characteristic of the tumor microenvironment, these NPs undergo a conformational change that facilitates the release of thrombin, which in turn catalyzes the internalization of cRGD-pro(S) nanomedicine into the neoplastic cells. Intracellularly, the cRGD-pro(S) nanomedicine is designed to release the cytotoxic SN38 in response to the glutathione-enriched environment. Thrombin, in its activated state, facilitates the conversion of fibrinogen to fibrin, thereby inducing rapid aggregation of erythrocytes and the formation of thrombi. These thrombi obstruct the tumor vasculature, leading to ischemic tumor starvation. Subsequently, SN38 exerts its cytotoxic effects, effectively annihilating the neoplastic cells (Scheme 1).

The amphiphilic polymeric prodrug of cRGD-PEG-PLys(ss-SN38) [cRGD-pro(S)] was synthesized in accordance with the synthetic pathway delineated in Fig. 1. Initially, the terminal carboxyl group of HOOC-PEG-NH-BOC underwent activation *via* 1-ethyl-3-(3-dimethylaminopropyl)carbodiimide hydrochloride (EDC·HCl) and N-Hydroxysuccinimide (NHS), facilitating the formation of an active ester intermediate. Subsequently, the cRGDfK moiety was covalently appended to the primary



Scheme 1 Diagrammatic illustration of dual prodrug nanomedicine for polypharmacological strategies for anti-tumor therapy of triple negative breast carcinoma. The proposed multifaceted nanomedicine was tailored to afford not only spatiotemporal responsiveness to the unique acidic pH and reductive potential of the triple-negative breast cancer microenvironment, enabling targeted release and enhanced therapeutic efficacies. Importantly, the pharmacokinetic and pharmacodynamic profiles within the tumor microenvironment, including the stimulated tissue extravasation and the durable containment of the chemotherapeutics, precipitated by strategically thrombin-mediated vasculature occlusion, could significantly amplify the therapeutic efficacies of the chemotherapeutic drugs

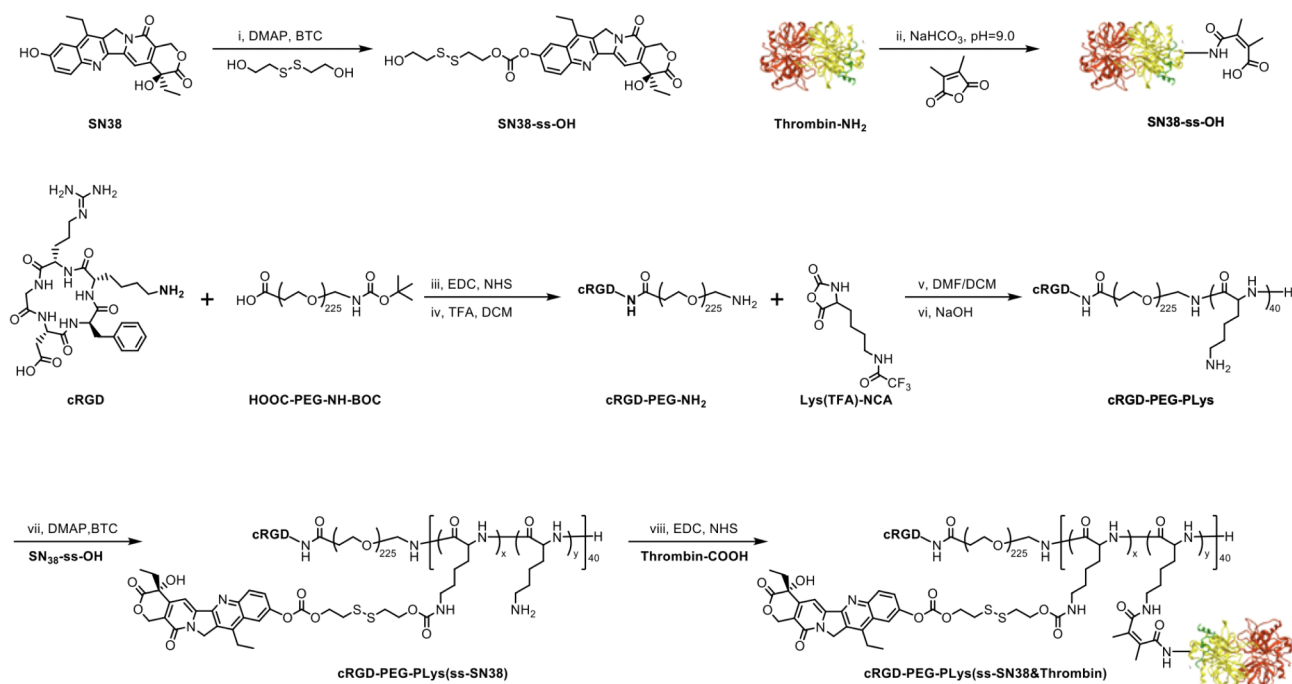


Fig. 1 Synthetic route of the dual prodrug nanomedicine comprising SN38 and thrombin

amine terminus of cRGDfK, yielding cRGD-PEG-NH(-BOC). Subsequently, this intermediate was then subjected to Boc group deprotection, resulting in the free amine form cRGD-PEG-NH₂. Further polymerization into PLys was achieved through ring-opening polymerization of monomer of Lys(TFA)-NCA, initiated by the terminal amine group of cRGD-PEG-NH₂. The subsequent alkaline hydrolysis of TFA residues yielded the block copolymer cRGD-PEG-PLys. Notably, the synthetic PLys segments were characterized by a polymerization degree of approximately 40.0 (Fig. S1), as determined by proton nuclear magnetic resonance spectroscopy, with the lysine unit's amino groups being poised for the subsequent covalent attachment of chemotherapeutic SN38 components.

In pursuit of a labile attachment of SN38 components, a low molecular weight SN38 prodrug (SN38-ss-OH), endowed with a redox-responsive cleavable disulfide linkage, was synthesized via triphosgene-mediated condensation between the hydroxyl group of SN38 and 2,2'-dithiodiethanol. The resultant product was characterized by mass spectrometry (Fig. 2a) and ¹H-NMR (Fig. 2b), with the ¹H NMR spectrum of SN38-ss-OH being quantitatively consistent with its chemical structure. The purity and molecular weight of the product were further confirmed by high-performance liquid chromatography (HPLC) (Fig. S2) and mass spectrometry, respectively.

Subsequently, the synthesized SN38-ss-OH was conjugated to the amino groups of the lysine units in PEG-PLys

to form a carbonate linkage, mediated by triphosgene. The resulting PEG-PLys(ss-SN38) was anticipated to be responsive to the intracellular reducing environment, liberating active SN38 through a disulfide-cleavage-mediated thiolcyclization reaction (Scheme 1). The successful conjugation of SN38 to the PLys segment was confirmed by both ¹H NMR and Fourier-transform infrared spectroscopy (FT-IR, Thermo Scientific Nicolet iS5, Waltham, MA) (Fig. 2c). Peaks at approximately 8.5–7.5 ppm, attributed to the aromatic protons of SN38, were identified in the ¹H NMR spectrum (solvent: CDCl₃) of PEG-PLys(ss-SN38), and the number of SN38 molecules per PEG-PLys(ss-SN38) was estimated to be approximately 12.0 accordingly. Additionally, HPLC analysis of the synthesized cRGD-PEG-PLys(ss-SN38) revealed no detectable free SN38 or SN38 derivatives (Fig. 2e). Concurrently, the FT-IR spectrum of PEG-PLys(ss-SN38) (Fig. 2d) displayed an emerging absorption at 1750 cm⁻¹, indicative of the C=O stretching vibrations in the esterification of the SN38 derivative (SN38-ss-), thereby further corroborating the successful preparation of PEG-PLys(ss-SN38).

The critical aggregation concentration (CAC) of cRGD-pro(S) was determined to be approximately 0.035 mg/mL using a classical pyrene fluorescence assay [25], indicative of remarkable colloidal stability even upon substantial dilution in systemic administration (Fig. 3a). Dynamic light scattering (DLS) measurements revealed that cRGD-pro(S), devoid of thrombin, exhibits a hydrodynamic diameter of approximately 73.6 nm (Fig. 3b),

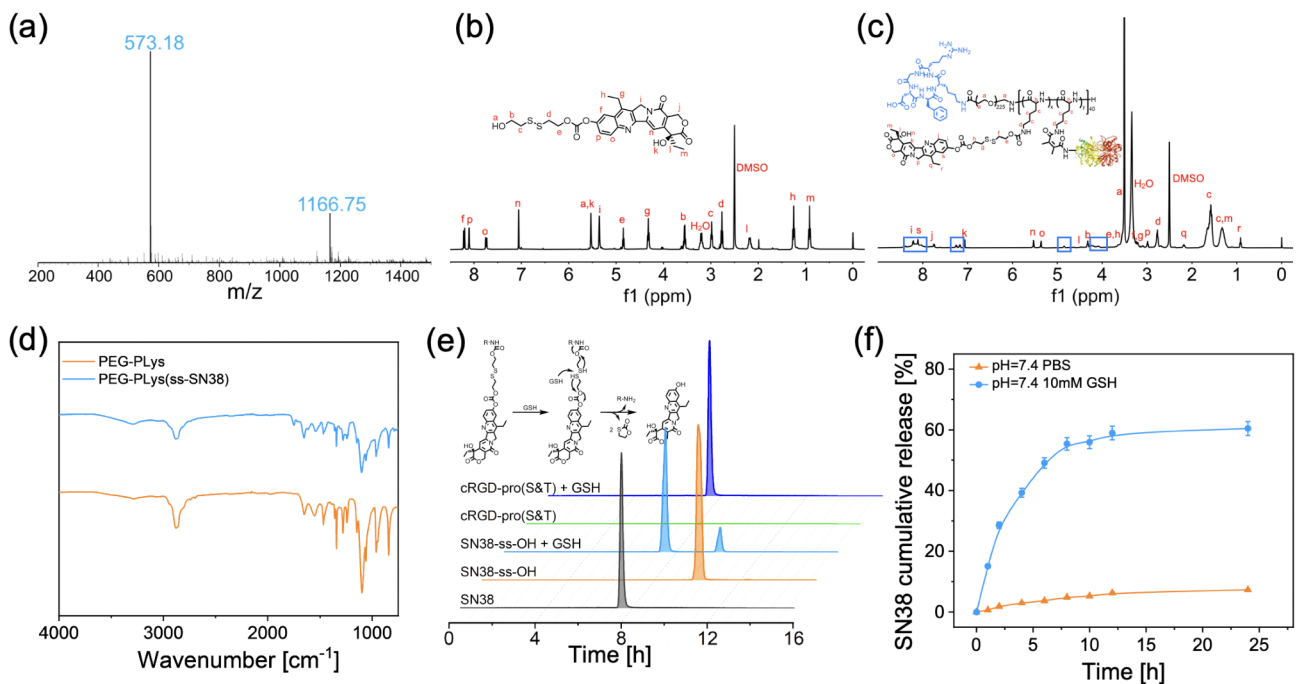


Fig. 2 Redox responsiveness of SN38-prodrug nanomedicine. **(a)** Mass spectrum for the synthesized prodrug of SN38-ss-OH; **(b)** ^1H NMR spectrum of the synthesized prodrug of SN38-ss-OH; **(c)** ^1H NMR spectrum of the synthesized polymeric prodrug of cRGD-PEG-Plys(ss-SN38&T); **(d)** FT-IR spectra of PEG-Plys and PEG-Plys(ss-SN38); **(e)** HPLC measurement for estimation of GSH-stimulated activation of SN-38 prodrugs; **(f)** Real time drug release of SN38 from cRGD-pro(S&T) nanomedicine in presence or absence of GSH (10 mM)

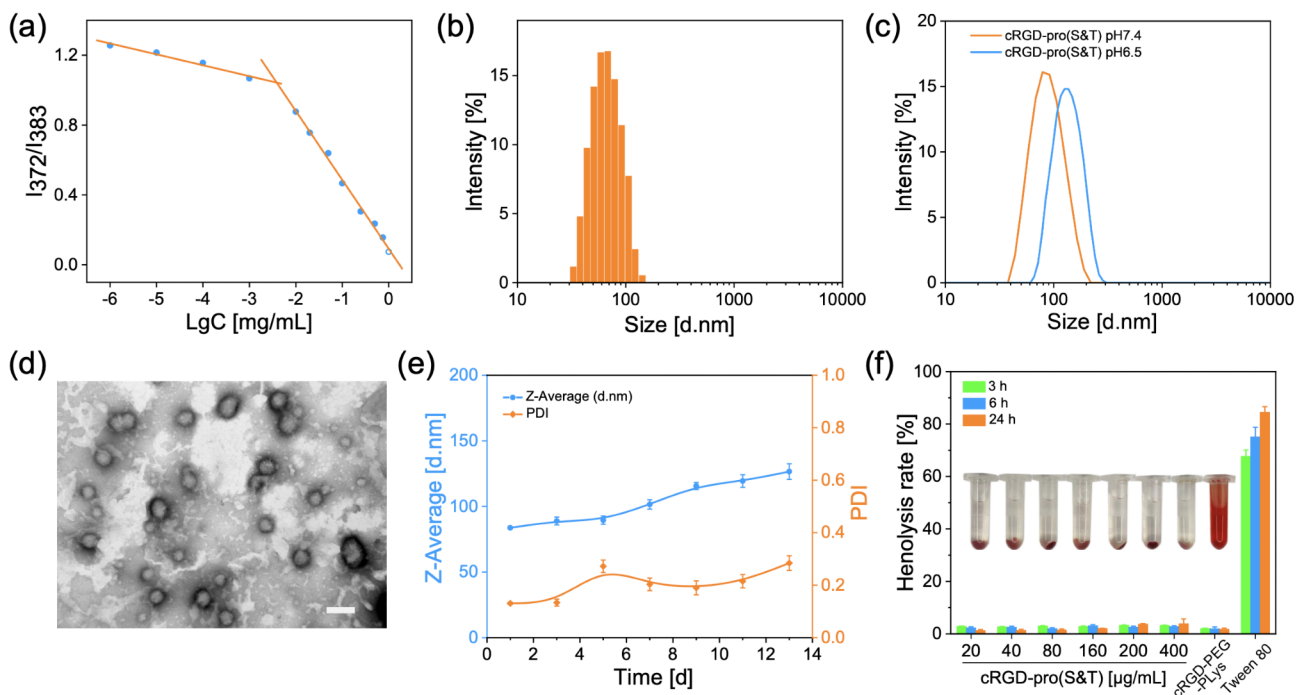


Fig. 3 Physicochemical properties of a variety of prodrug nanomedicine. **(a)** CMC assay for amphiphiles of cRGD-PEG-Plys(ss-SN38); **(b)** DLS measurement for cRGD-pro(S); **(c)** DLS measurement for cRGD-pro(S&T) in different pH buffers (pH 7.4 and 6.5); **(d)** Microscopic morphologies of cRGD-pro(S&T); **(e)** Time-dependent DLS measurement for cRGD-pro(S&T). Scale bar: 100 nm; **(f)** hemolytic activities of cRGD-pro(S&T) (insert: the hemolysis images after 24 h)

whereas cRGD-pro(S&T), laden with the thrombin payloads, exhibit a diameter of approximately 83.4 nm (Fig. 3c). Furthermore, insights into the hydrodynamic profile of thrombin and cRGD-pro(S&T) by fluorescence correlation spectroscopy measurement confirmed the readily accommodation of thrombin into nanomedicine (Fig. 4d), as evidenced by drastic retarded diffusion constant of cRGD-pro(S&T) (solid green line, wherein the thrombin was labelled with Cy5) in relative to the molecular thrombin. Particularly, the diffusion constant of cRGD-pro(S&T) was determined to be comparable to cRGD-pro(S). However, upon incubation at pH 6.5, reflective of the tumor microenvironment, the cRGD-pro(S&T) demonstrated a relative increase in hydrodynamic size to approximately 135.2 nm (Fig. 3c), suggesting the diminished interactions between the thrombin prodrug and cRGD-pro(S) components due to the decarboxylation of the thrombin prodrug. Transmission electron microscopy (TEM) measurements confirmed the uniform spherical morphologies of cRGD-pro(S&T), with particle diameters in the range of 70–80 nm. The relative discrepancy in size between TEM and DLS measurements is attributed to the dehydration effects during TEM specimen preparation (Fig. 3d). Furthermore, the colloidal stability of cRGD-pro(S&T) NPs was substantiated by the maintenance of constant size and polydispersity index (PDI) upon prolonged

incubation in phosphate-buffered saline (PBS) for approximately 14 days at 4 °C (Fig. 3e).

On the other hand, the primary amine groups of thrombin were strategically subjected carboxylation reaction with CAA for yielding carboxyl groups, with the intention of the facilitated binding of the thrombin prodrug to the lysine units of the aforementioned cRGD-PEG-PLys(ss-SN38) prodrug. The successful carboxylation was confirmed by ζ potential measurement, as evidenced by the substantial decline in ζ potential from -7.2 mV (the native thrombin prior to carboxylation) to -16.4 mV (the thrombin prodrug post carboxylation) (Fig. 4a). Of note, the strategic carboxylation was designed to be readily cleavable upon treatment in the tumoral acidic microenvironment, therefore, the subsequent decarboxylation is conjectured to be capable of restoring the original thrombin, consequently liberation of active thrombin could be speculated to be responsive to the mild tumor acidic stimuli.

To determine the acid-catalyzed release of thrombin from cRGD-pro(S&T) nanoparticles, we utilized S-2238, a colorimetric substrate, in an assay designed to quantify the activation and subsequent liberation of thrombin. In an effort to obviate potential absorbance interference attributable to the presence of SN38, we specifically formulated cRGD-pro(T) nanoparticles that were devoid of SN38 constituents for this investigation. In contradistinction to the negligible reaction observed for cRGD-pro(T)

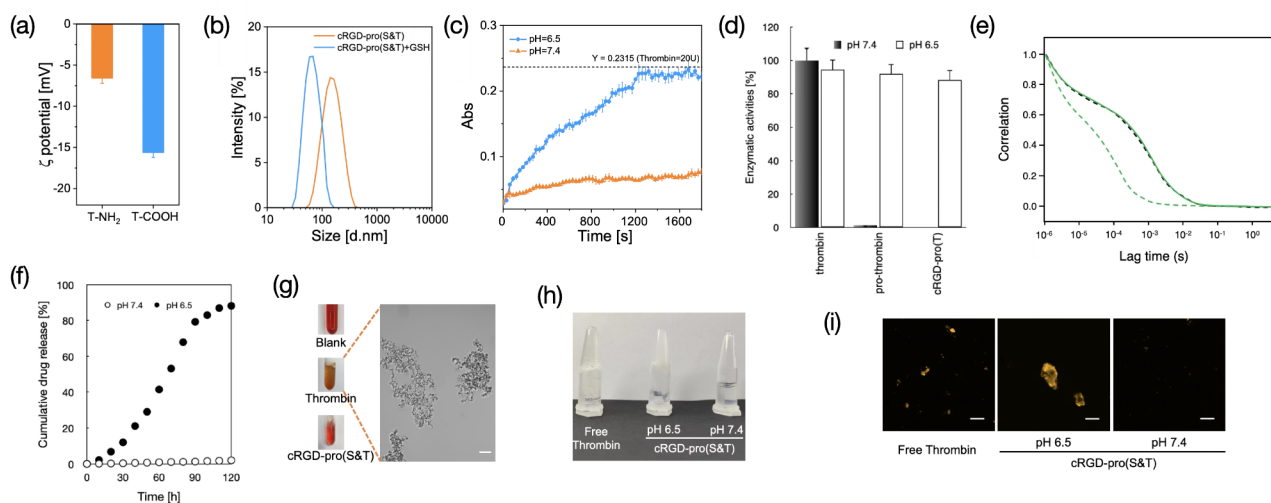


Fig. 4 pH responsiveness of thrombin prodrug nanomedicine. **(a)** ζ potential of thrombin prior to or post carboxylation reaction with CAA; **(b)** DLS measurement for cRGD-pro(S&T) in presence or absence of GSH (10 mM); **(c)** Time dependent measurement for estimation of activation of thrombin prodrug at pH 7.4 or 6.5; **(d)** Quantitative assessment of the enzymatic activities of thrombin following carboxylation and encapsulation, after 60-minute incubation at pH 7.4 or 6.5, based on its specific reaction with the chromogenic substrate S-2238. Data are presented as mean \pm SD ($n = 4$); **(e)** FCS measurement for thrombin upon complexation into cRGD-pro(S&T). Dashed green line: thrombin; Dashed black line: cRGD-pro(s); Solid green line: cRGD-pro(S&T); **(f)** Time-dependent release profile of thrombin from cRGD-pro(S&T) upon incubation at pH 7.4 or 6.5; **(g)** Investigations of the coagulation dynamics in sterile defibrinated sheep blood exposed to thrombin and cRGD-pro(S&T) nanomedicine; **(h)** Quantitative assessment of thrombin activity and comparative analysis of cRGD-pro(S&T) at mild acidic (pH 6.5) and neutral (pH 7.4) conditions post incubation with fibrinogen; **(i)** CLSM measurements for insights into coagulation of Cy3-labeled fibrinogen upon treatment with thrombin and cRGD-pro(S&T) at mild acidic (pH 6.5) and neutral (pH 7.4) milieu

nanoparticles at a physiological pH of 7.4 (as depicted in Fig. 4c, d), a monotonic increase in absorbance, signifying the enzymatic reactions between S-2238 and active thrombin, was detected upon incubation of cRGD-pro(T) nanoparticles under acidic conditions (pH 6.5). This observation infers that within the moderately acidic milieu of the tumor microenvironment, the covalent bonds anchoring the thrombin within the nanomedicine are prone to decarboxylation. This chemical alteration is postulated to expedite the release of the coagulation enzyme (Fig. 4d), as evidenced by the comparable diffusion time of nanomedicine (containing fluorescence-labeled pro-thrombin) at pH 6.5 by FCS measurement to the native thrombin. Consequently, the progressive release of the active thrombin was accomplished (Fig. 4f, Fig. S5), culminating in the resumption of its enzymatic function and a concomitant swift reaction with the luminescent substrate. It is noteworthy that no appreciable alteration in absorbance was recorded at pH 7.4, thereby corroborating the pH-responsive profile of thrombin release. This result underscores the precision of the nanoplateform's pH-triggered release mechanism, which is of importance for ensuring that the thrombin release is confined to the acidic tumor microenvironment, thus minimizing systemic activation and potential off-target effects.

Furthermore, we executed comprehensive investigations into the coagulation phenomena (as illustrated in Fig. 4g-i), thereby highlighting the intrinsic capability of cRGD-pro(T) to exert the release of the biologically active thrombin in response to the pH gradient that is quintessential to the tumor microenvironment, specifically at a pH of 6.5. This orchestrated biochemical cascade culminates in the pronounced aggregation of fibrinogen, which subsequently incites interactions with erythrocytes, leading to the precipitation of thrombi formation.

Subsequently, hemolysis assays were conducted to ascertain the biocompatibility profiles of the nanomaterials. These assessments demonstrated that these nanoconstructs exhibit an exemplary degree of biocompatibility and a minimal tendency to prematurely release thrombin payloads during systemic circulation (as referenced in Fig. 3f and Fig. S6, ESI⁺). This underscores the potential of these nanoplateforms to selectively induce thrombotic events within the tumor microenvironment while preserving systemic circulation integrity.

To this end, the findings collectively contribute to scientific rationale for the utilization of pH-responsive nanoplateforms in the targeted delivery of thrombin, offering a nuanced approach to modulating the tumor microenvironment and enhancing the therapeutic index of anticancer interventions.

Furthermore, to delineate the release kinetics of SN38 from the intricately designed cRGD-pro(S&T) prodrug nanomedicine in response to the intracellular redox milieu, a series of experimental assays was conducted, as portrayed in Fig. 2f. Under conditions mimicking physiological pH (7.4) and in the absence of glutathione (GSH), the liberation of SN38 was significantly impeded, accruing to a mere 9.1% over a 48-hour interval. In dramatic juxtaposition, the intracellular reductive microenvironment, augmented by the presence of GSH, was observed to markedly hasten the discharge of SN38, with the cumulative release rates soaring to approximately 64.1% within the aforementioned temporal frame. These findings substantiate the redox-responsive release mechanism of the cRGD-pro(S&T) prodrug nanomedicine, which is pivotal for ensuring the targeted delivery and controlled release of the chemotherapeutic agent SN38 specifically within the reductive tumor microenvironment. This precise spatiotemporal control over drug release is anticipated to augment the therapeutic index and attenuate systemic toxicities associated with conventional chemotherapy regimens.

Considering the intrinsic aggregation-induced quenching effect of SN38, we deployed real-time confocal laser scanning microscopy (CLSM) to scrutinize the intracellular trafficking and liberation of SN38, visualized in blue fluorescence. Concurrently, the endolysosomal structures were delineated in green. The cRGD-pro(S) nanoparticles were co-cultured with MCF-7 cells for a duration of 2 h, succeeded by a rigorous washing protocol employing PBS to meticulously eliminate any extracellular cRGD-pro(S). As depicted in Fig. 5a and Fig. S7, an initial paucity of SN38 fluorescence was observed during the nascent phase (e.g., 2–6 h, Fig. 5b). Subsequently, a monotonic amplification in the fluorescence intensities of SN38 was monitored up to a 24-hour interval (Fig. 5c). The initially diminished fluorescence of SN38 is ascribable to the aforementioned quenching phenomenon occurring when the molecule is chemically confined within the nanomedicine constructs. However, upon encountering the intracellular milieu rich in glutathione, the covalent bond anchoring the SN38 prodrug was severed, precipitating the molecular dispersion of SN38 and a concomitant resumption of its fluorescence.

Of particular note, SN38 was predominantly ensconced within the endolysosomal compartments during the early phase (2–6 h). Yet, as the temporal continuum progressed, the dispersion of SN38 throughout the cytosol became increasingly apparent, indicative of its activation and liberation from the nanomedicine, coupled with a translocation from the endolysosomal confines. Ultimately, after a 36-hour incubation period, a pronounced accumulation of SN38 within the target nuclei was

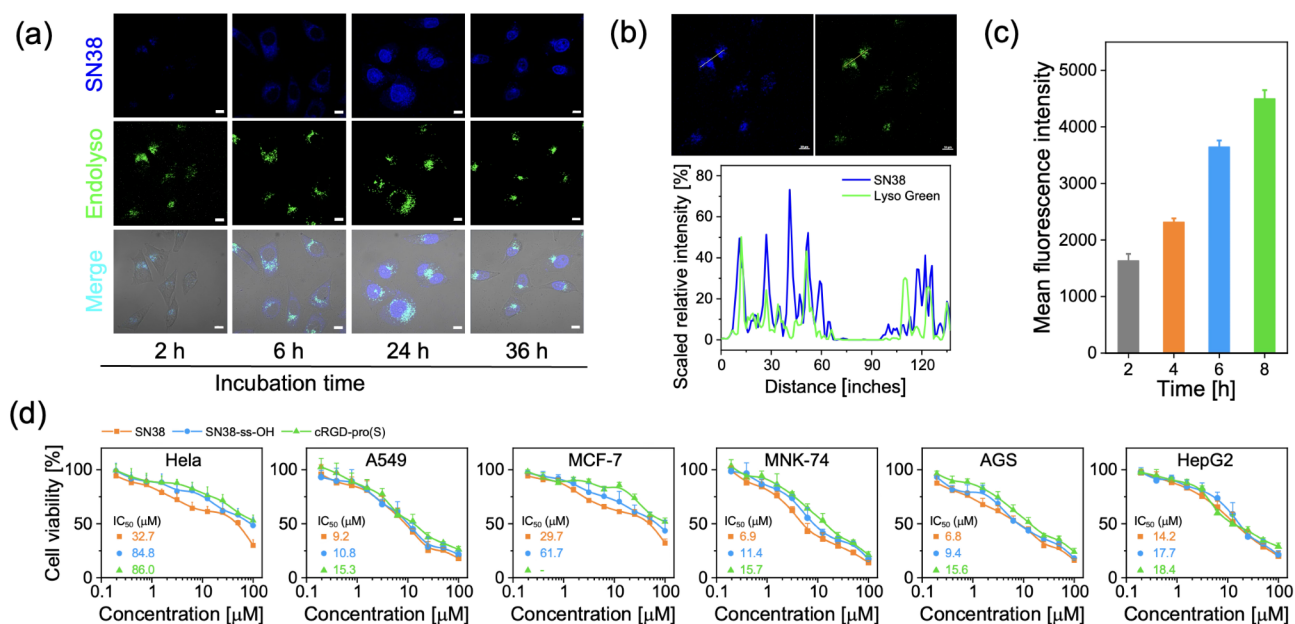


Fig. 5 In vitro biological performance of a variety of prodrug nanomedicine. (a) Real time CLSM measurement for tracing intracellular trafficking of SN38; (b) Detailed analysis in pertinent of the intracellular distribution of SN38 and endolysosomes at 2 h; (c) Time dependent measurement for quantification of the intercellular fluorescence intensities of SN38; (d) Cytotoxic potencies of a variety of SN38 therapeutics against a panel of cancerous cells

observed, positioning it to exert its chemotherapeutic action by inhibiting topoisomerase I.

Hence, the CLSM analysis provides compelling visual evidence of the intracellular dynamics of the cRGD-pro(S&T) nanomedicine, elucidating the spatiotemporal control over the release and activation of SN38, which is paramount for optimizing its chemotherapeutic efficacies while minimizing the unfavorable systemic side effects.

In the ensuing in vitro studies, the cytotoxic efficacy of the aforementioned nanomedicine was evaluated against a panel of malignant cell lines. The cytotoxic potential of the active moiety, SN38, was discerned to be substantially retained despite the intricate procedures of prodrug synthesis and subsequent encapsulation within the nanoscale delivery system, and their IC_{50} index was determined to be in the range of several tens nanomole (Fig. 5d). This retention of potency is indicative of the nanomedicine's redox-responsive properties, which are maintained without a concomitant reduction in its cytotoxic capabilities.

Contrasting with the conventional paradigm where nanoencapsulated chemotherapeutic agents are often perceived to exhibit attenuated cytotoxicity relative to their unmodified counterparts, this is predominantly due to the impediments encountered in cellular internalization and the suboptimal intracellular drug release kinetics. However, the pronounced cytotoxic potency observed in our investigation suggests that the innovative design of the nanomedicine, which encompasses the utilization of RGD peptide-mediated cellular uptake and a redox-triggered intracellular drug liberation

mechanism, effectively surmounts these biological barriers and augments the therapeutic index of SN38. This approach underscores the potential of our nanoformulation to transcend the limitations inherent in traditional nanomedicines, thereby offering a promising avenue for enhanced cancer therapeutics.

To systematically evaluate the in vivo antitumor efficacies of cRGD-pro(S&T) nanoparticles, a xenografted solid tumor model employing human breast cancer MCF-7 cells was established. The chemotherapeutic regimens were administered in accordance with the protocol delineated in Fig. 6a. The dual prodrug nanomedicine exhibited unparalleled potency in the suppression of tumor growth, as evidenced in Fig. 6b and c. In stark contradistinction, the PBS control group demonstrated a relentless increase in tumor volume, escalating from 50 mm^3 to approximately 477 mm^3 . The cRGD-pro(T) group manifested a modest inhibition of tumor growth, culminating in a final tumor volume of 375 mm^3 , whereas the SN38 group displayed a moderate inhibition, with a final tumor volume of 186.4 mm^3 . Nonetheless, the combinatorial therapy groups administered with pro(S&T) and cRGD-pro(S&T) significantly impeded the tumor growth, demonstrating the most potent antitumor efficacies, with the mean tumor volumes of approximately 94 mm^3 and 23 mm^3 , respectively.

Furthermore, we have conducted additional anti-tumor experiments involving four groups: PBS, cRGD-pro(S), cRGD-pro(S&T), and cRGD-pro(S&A) (where A denotes pro-Albumin devoid of therapeutic activity). These experiments were designed to elucidate the

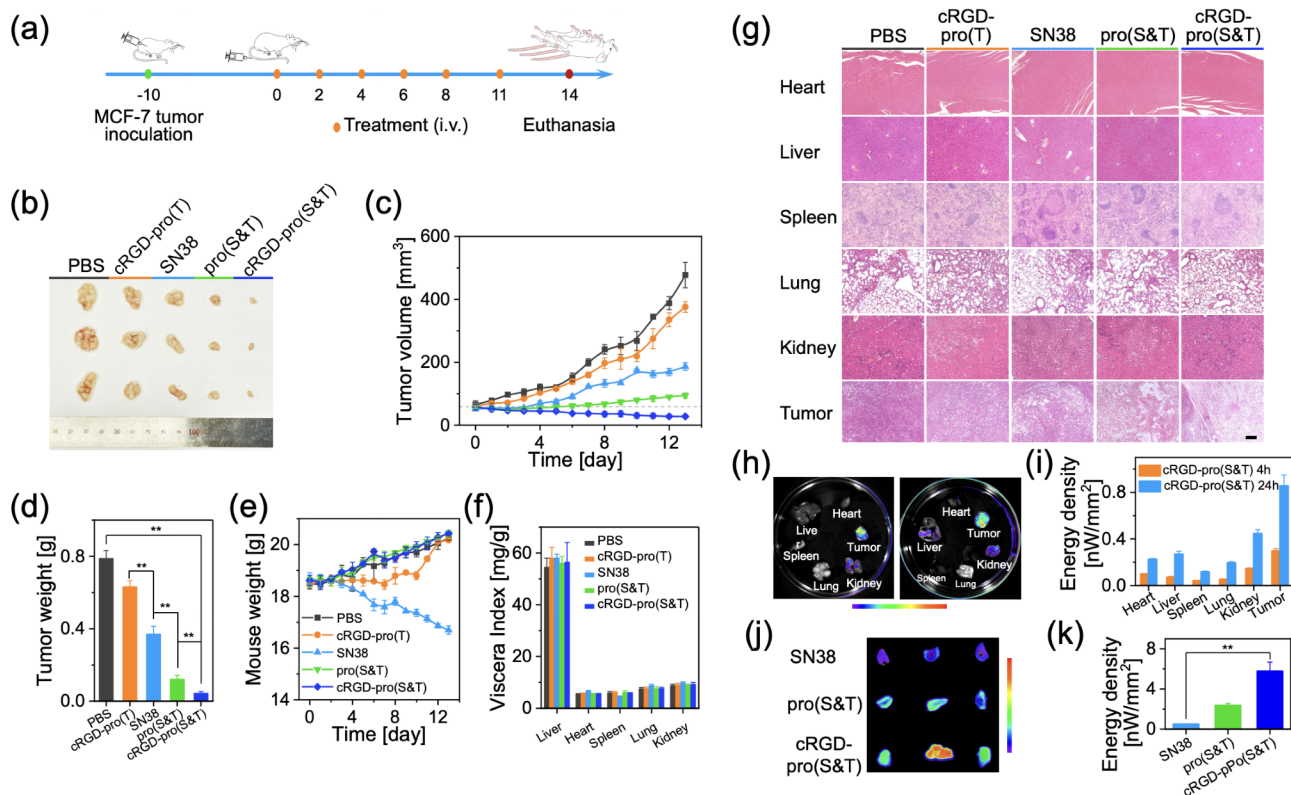


Fig. 6 In vivo antitumor efficacies of prodrug nanomedicines in a systemic therapy model of TNBC. **(a)** Schematic depiction of the systemic therapeutic regimen for TNBC; **(b)** Morphometric analysis of excised neoplastic tissues at the termination of treatment; **(c)** Comparative efficacy of tumor growth suppression upon systemic administration; **(d)** Quantitative assessment of tumor mass at the conclusion of the therapeutic course [$n=3$, mean \pm s.e.m., $**p < 0.01$ (student t test)]; **(e)** Serial monitoring of body mass indices throughout the treatment period; **(f)** Determination of visceral indices for a spectrum of therapeutic agents at 24 h post intravenous administration; **(g)** Histological examination via Hematoxylin and Eosin staining to evaluate the histopathological integrity of various organ systems, with a reference scale bar indicated at 100 micrometers; **(h)** Ex vivo analysis elucidating the biodistribution of cRGD-pro(S&T) nanoconstructs at 4 and 24 h post-intravascular injection, with a corresponding quantitative analysis summarized in **(i)**; **(j)** Comparative quantification of tumor accumulation efficacy for a panel of SN38-laden constructs at 24 h post intravenous administration, with a comprehensive quantitative analysis summarized in **(k)** [$n=3$, mean \pm s.e.m., $**p < 0.01$ (student t test)]

functional contribution of thrombin. As illustrated in Fig. S8, the cRGD-pro(S) chemotherapeutic nanomedicine effectively suppressed tumor growth. Notably, the role of thrombin in augmenting anti-tumor efficacy was clearly demonstrated, as evidenced by the significantly lower tumor growth rates observed in the cRGD-pro(S&T) group compared to the cRGD-pro(S) group. Moreover, the comparable anti-tumor efficacy between cRGD-pro(S) and cRGD-pro(S&A) further supports the conclusion that the enhanced efficacy of cRGD-pro(S&T) is largely attributable to the functional activities of thrombin.

Upon completion of the treatment regimen, the weight of each tumor mass was measured (as depicted in Fig. 6d), and the tumor inhibition rates were calculated, yielding approximately 21.3%, 61.0%, 80.1%, and 91.9% for the cRGD-pro(T), SN38, pro(S&T), and cRGD-pro(S&T), respectively. Hence, thrombin starvation therapy appeared to be a potent approach to the modulation of tumor angiogenesis by inducing thrombosis and

impairing the formation and function of tumor vasculature. This strategy is believed to elicit vascular degeneration and ischemia within the tumors, thereby inhibiting tumor growth and metastasis.

In terms of the overall safety profiles, the SN38 group exhibited significant systemic toxicities, as evidenced by the pronounced decline in body weight (as illustrated in Fig. 6e). Notably, the average weights of the spleens were determined to have diminished by approximately 20% (as shown in Fig. 6f). It is postulated that the insoluble SN38 has a propensity to aggregate into large micrometer-scaled particles, which are subsequently sequestered by the spleens. Moreover, histopathological examination via hematoxylin and eosin (H&E) staining corroborated severe damage to vital organs in mice under systemic treatment with SN38 (Fig. S9). In stark contrast, no discernible systemic toxicities were detected in other groups administered the nanomedicine, as referenced in Fig. 6g. Hence, the proposed dual prodrug nanomedicine emerges as a promising candidate, offering as an

intriguingly safe and efficacious therapeutic strategy for cancer treatment.

It is of particular interest to observe that the augmented tumoral deposition of our cRGD-conjugated nanomedicine was validated. The serial accumulation within neoplastic tissues, as delineated in Fig. 6h and i, is evidenced by a statistically significant elevation in the nanomedicine concentration at the 24-hour time point relative to the earlier 4-hour time point. Notably, at the 24-hour post-intravascular administration, the cRGD-pro(S&T) construct exhibited a pronounced affinity for tumoral accumulation, which was not only superior to that observed in other major organs, particularly exceeding deposition levels in the livers, an organ traditionally characterized by a high density of the reticuloendothelial system (RES), including Kuffer's cells.

In stark contrast, the nanomedicine lacking the cRGD targeting ligand demonstrated a significantly attenuated tumoral accumulation efficacies, as quantified in Fig. 6j and k. Despite this, the accumulation was still found to be substantially greater than that of the molecular SN38, a finding that is congruent with the extant literature which posits that nanomedicines with tailored physiochemical properties can achieve enhanced tumoral deposition secondary to the enhanced permeability and retention (EPR) phenomenon intrinsic to solid neoplasms.

Furthermore, to elucidate the synergistic therapeutic mechanisms underpinning the dual prodrug nanomedicine, an exhaustive immunofluorescent staining analysis was conducted on neoplastic tissues (as depicted in Fig. 7a). The cellular nuclei were selectively labeled with 4',6'-diamidino-2-phenylindole (DAPI; pseudo-colored blue), while the tumor vasculature was demarcated with cluster of differentiation 31 (CD31; pseudo-colored green). A comparative assessment revealed that thrombin-enriched groups—cRGD-pro(T), pro(S&T) and cRGD-pro(S&T)—uniformly demonstrated diminished neovessel densities (green) when juxtaposed against the PBS control group (as illustrated in Fig. 7a and b).

Further corroboration was provided by hematoxylin and eosin (H&E) staining (as shown in Fig. 6g), indicating that while tumor starvation therapy alone exhibited limited anti-neoplastic efficacies, the dual prodrug nanomedicines pro(S&T) and cRGD-pro(S&T), in stark contrast to the chemotherapy cohort treated with SN38, displayed a pronounced reduction in vascularity. The histologic examination via H&E substantiated the potent anti-neoplastic efficacies, confirming that the synergistic therapeutics of the dual prodrug nanomedicine can effectively abrogate tumor angiogenesis. This action severs the nutrient conduit to neoplastic tissues, inducing a state of starvation and vulnerability, which in turn augments the therapeutic outcomes through the subsequent release of chemotherapeutics.

To quantitatively evaluate the impact of occlusive mechanisms on perfusion impairment, we assessed the intratumoral red blood cell concentration. The subsequent results indicated significant reduction in the intratumoral volume of hemoglobin per unit volume in the cohort treated with thrombin (as illustrated in Fig. 7c). It is hypothesized that, following the release of thrombin within the tumoral compartment, the endogenous fibrinogen rapidly polymerizes into fibrin, culminating in vascular occlusion and subsequent impediment of blood supply. This occlusive mechanism is posited to further enhance the therapeutic efficacy of the nanomedicine by creating a localized hypoxic environment that is inimical to tumor survival and growth.

Additionally, the augmented permeation of therapeutics throughout the neoplastic stroma is hypothesized to result from the targeted vasculature occlusion, which may precipitate substantial cell mortality predicated on chemotherapeutic action. It is acknowledged that clinical tumor vessel embolization represents a widely implemented therapeutic strategy within oncological practice^{23, 24}. This procedure functions by obstructing the arterial inflow to the tumor mass, thereby instigating ischemia and hypoxia within the oncotic tissue, ultimately culminating in oncotic necrosis.

This methodological intervention not only elevates the concentration of therapeutic agents at the local site and extends the temporal duration of interaction between the drug and the tumoral tissue but also attenuates the intratumoral pressure through the abridgement of intratumoral trafficking. This reduction in pressure subsequently augments the permeability of the therapeutic agents.

Note that the conventional macroscopic analysis of drug distribution within biological matrices has been predicated upon the homogenization of tissue samples, followed by quantification via Liquid Chromatography-Mass Spectrometry (LC-MS) or its tandem variant (LC-MS/MS). While these methodologies have been instrumental in facilitating absolute quantification, they are inherently incapable of discerning the intracellular and extracellular microdistribution of the pharmaceutical agents post-homogenization.

Conversely, Matrix-Assisted Laser Desorption/Ionization Mass Spectrometry Imaging (MALDI MSI) transcends these limitations by affording high-resolution spatial mapping [20]. This technique facilitates the precise localization of the analyte of interest at discrete anatomical coordinates within a tissue section. Consequently, MALDI MSI enables the elucidation of the micro-scale pharmacokinetic processes, thereby providing an unprecedented level of details regarding the drug's transport and distribution within the intricate micro-environments of the tissues [26, 27]. Such granularity is

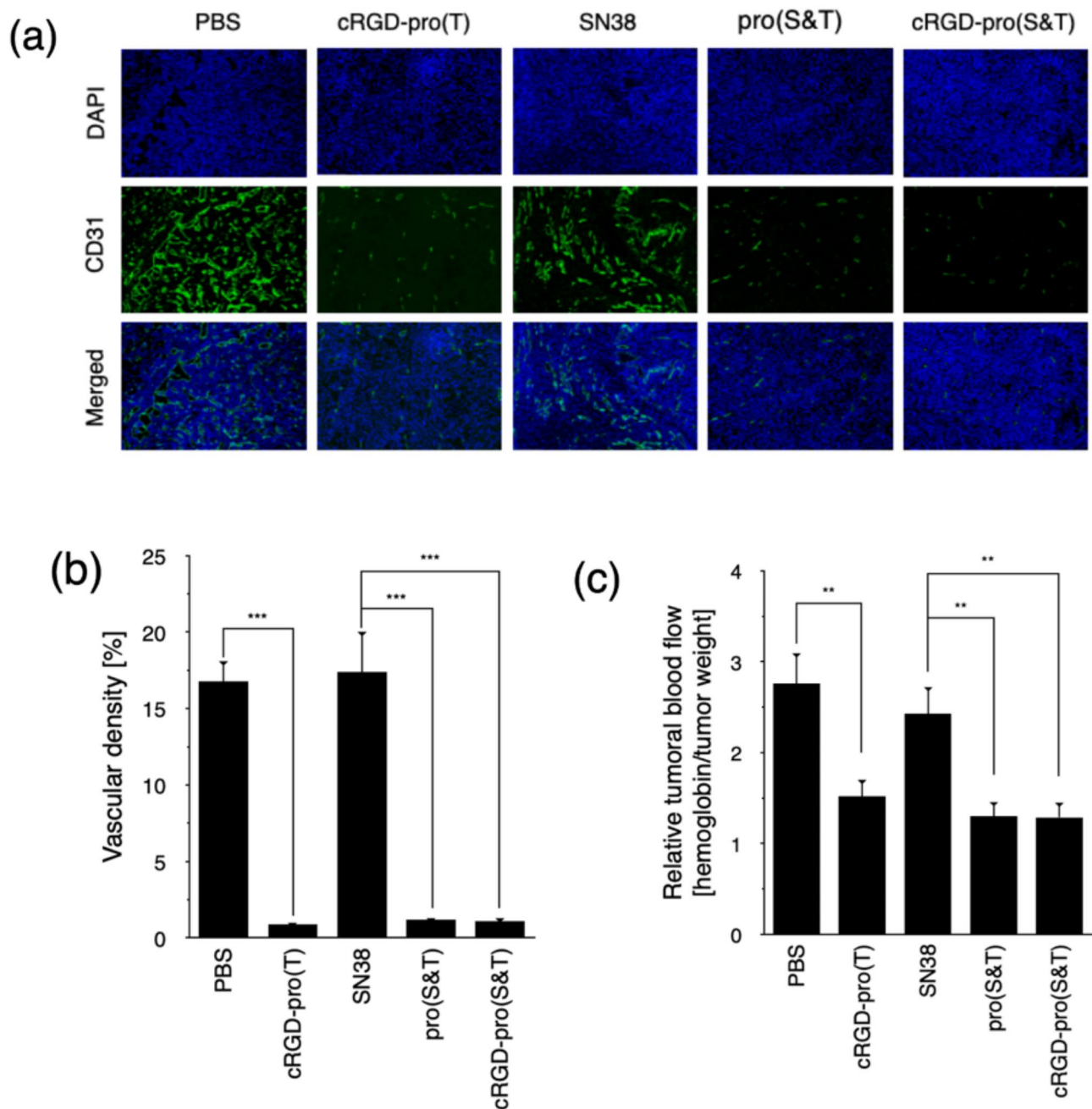


Fig. 7 Investigations of amplified anti-tumor efficacies by strategic integration of the vasculature-clotting thrombin into prodrug nanomedicine. **(a)** CLSM images of immunostaining of tumoral blood vessels post systemic treatment (14 days) of a variety of nanomedicine; **(b)** Quantified vascular densities upon systemic treatment of a variety of nanomedicine (14 days) [$n=4$, mean \pm s.d., *** $p < 0.001$ (student t test)]; **(c)** Quantification of the red blood cells in tumors by means of quantitative measurement of hemoglobin per tumor (14 days). [$n=4$, mean \pm s.d., ** $p < 0.01$ (student t test)]

paramount for advancing our comprehension of the spatiotemporal dynamics of drug action and its ramifications for therapeutic efficacy and safety profiles.

As illustrated in Fig. 8b, the nanomedicine lacking the vasculature-clotting moiety of thrombin exhibited a restricted transvascular penetration into the tumoral stroma. Particularly, the preponderance of the nanomedicine was observed to be sequestered within the vascular

channels or fibrotic regions. This observation may be potentially elucidated by the well-established elevated internal pressure of the tumor, which impedes effective extravasation into the tumoral nests (Fig. 8c and d). In contradistinction, the nanomedicine that incorporated the vasculature-clotting component of thrombin displayed a remarkably homogeneous distribution across the entire tumoral mass.

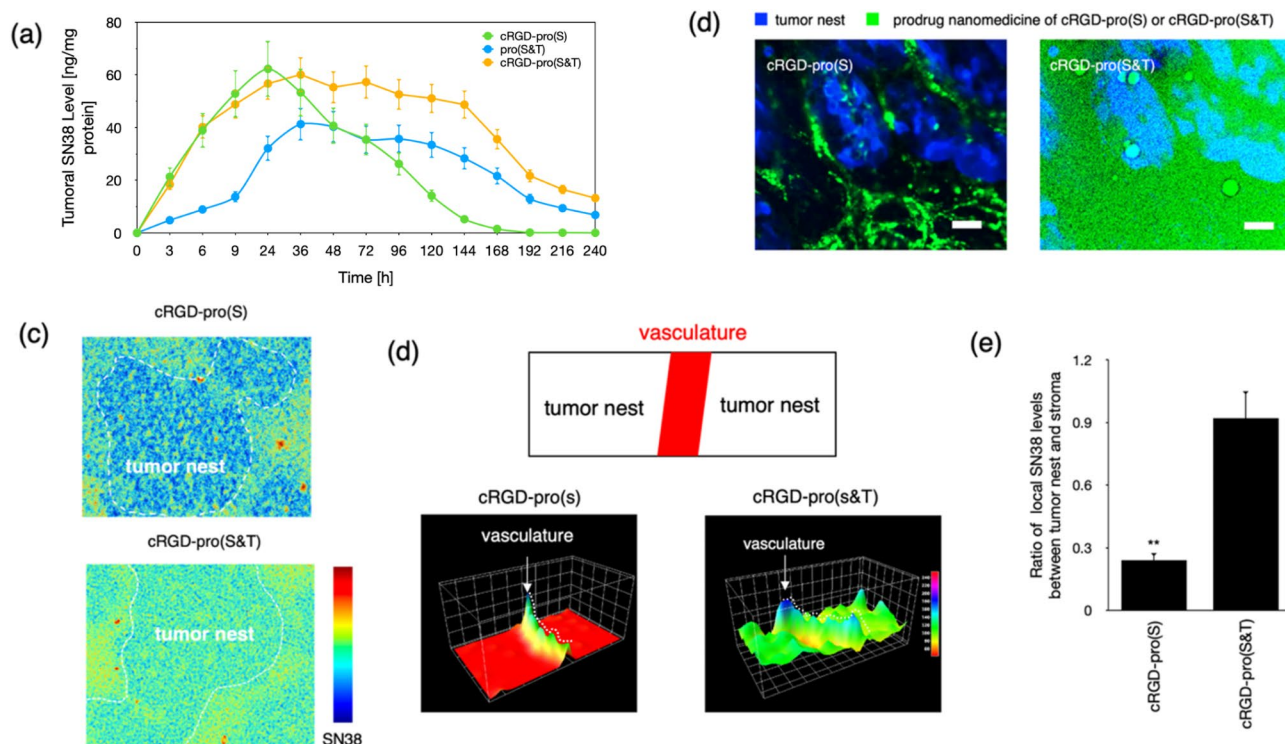


Fig. 8 Insights into the intratumor pharmacokinetic and pharmacodynamic by strategic integration of the vasculature-clotting thrombin into the prodrug nanomedicine ($n=3$, mean \pm s.d.). **(a)** SN38 retention in tumors as a function of time upon dosage of a variety of nanomedicine; **(b)** Intratumor distributions of prodrug nanomedicine of cRGD-pro(s) or cRGD-pro(S&T); **(c)** Mass spectrometry mapping for assessment of intratumor distributions of chemotherapeutic SN38 upon systemic treatment of cRGD-pro(s) or cRGD-pro(S&T); **(d)** Illustration of intratumor distributions of chemotherapeutic SN38, wherein the relative levels of SN38 were expressed into 3D scattering plot; **(e)** The quantified ratios of SN38 between tumor nest and tumor stroma. [$n=6$, mean \pm s.d., ** $p < 0.01$ (student t test)]

A plausible etiology for this phenomenon is as follows: during the process of tumoral angiogenesis, the aberrant structural configuration of the tumoral vasculature, characterized by the enlarged pore dimensions, engenders an increase in the internal pressure of the tumor, thereby hindering the pervasion of pharmacological molecules. Nonetheless, the therapeutic intervention of anti-angiogenic vasculature-clotting can induce the normalization of tumoral vasculature, ameliorate the pore dimensions within the vascular walls, and thus reduce the intra-tumoral pressure. This reduction in pressure facilitates the passive transudation of therapeutics across the tumoral stroma. Consequently, it is inferred that the occlusion of tumor vasculature may diminish the internal pressure of the tumor, which aids in the amelioration of the delivery efficiency of chemotherapeutic agents.

In the realm of oncology, the targeted obliteration of tumor vasculature is projected to effectuate a significant augmentation of the spatiotemporal sequestration of chemotherapeutic agents within the neoplastic milieu. This sustained retention is anticipated to engender and perpetuate elevated concentrations of chemotherapeutic agents, thereby instituting a potent and protracted cytotoxic environment. Subsequent

quantification of intratumoral SN38 has validated our hypotheses, evidencing that nanomedicines incorporating vasculature-clotting thrombin constituents are capable of maintaining an elevated concentration gradient of SN38 for an extended period of 5–6 days (Fig. 8a), antecedent to a gradual decline. This enduring retention starkly contrasts with the precipitous decrement observed in nanomedicines lacking vasculature-clotting thrombin constituents, despite equivalent initial accumulations at the 24-hour juncture.

For instance, the relative concentration of SN38 at oncotic tissues was determined to be approximately 4.6-fold elevated for nanomedicines endowed with vasculature-clotting thrombin constituents relative to their non-thrombin counterparts (Fig. 8e). Consequently, the promoted tissue extravasation and the protracted retention of the chemotherapeutic SN38, precipitated by thrombin-mediated vasculature occlusion, could substantially amplify the therapeutic efficacies of SN38. This intensification in pharmacological potency is conjectured to contribute to the enhancement of anti-neoplastic efficacies.

Hence, the strategic incorporation of thrombin within nanomedicines emerges as a promising therapeutic

paradigm, enhancing the chemotherapeutic index by modulating the pharmacokinetic and pharmacodynamic profiles within the tumor microenvironment. This approach delineates an intriguing avenue for the augmentation of chemotherapeutic potencies, offering a nuanced strategy in the multifaceted battle against neoplastic diseases. In recent years, the combination of anti-VEGF antibodies with chemotherapy has shown significant promise in enhancing therapeutic efficacy across various cancers. For instance, a recent phase III clinical trial demonstrated that the combination of bevacizumab (an anti-VEGF antibody) with the XELOX chemotherapy regimen significantly improved progression-free survival (PFS) and overall survival (OS) in patients with metastatic colorectal cancer. This study highlights the synergistic effects of combining anti-angiogenic therapy with traditional chemotherapy, which aligns with our findings on the benefits of modulating the tumor vascular microenvironment to enhance drug delivery and therapeutic efficacy.

Another relevant study is the ARTEMIS-CTONG1509 trial, which investigated the combination of bevacizumab with the EGFR tyrosine kinase inhibitor erlotinib in patients with advanced EGFR-mutant non-small cell lung cancer (NSCLC). The results showed a significant extension of PFS from 11.2 months with erlotinib alone to 17.9 months with the combination therapy. This further underscores the potential of anti-VEGF antibodies to improve outcomes when used in conjunction with targeted therapies and chemotherapy.

These studies collectively emphasize the importance of modulating the tumor vascular microenvironment to enhance the delivery and effectiveness of chemotherapeutic agents. Consequently, the systematic studies provide profound insights into the multifaceted therapeutic mechanisms of the dual prodrug nanomedicine, which highlight the potential of this innovative approach as a promising therapeutic agent, particularly for neoplastic conditions marked by aggressive angiogenesis and resistance to conventional chemotherapy. The comprehensive understanding garnered from these investigations underscores the unique advantages of this nanomedicine in addressing the complex challenges posed by these diseases. By leveraging the synergistic effects of dual prodrugs and nanoscale delivery systems, this modality holds the promise of revolutionizing cancer treatment, offering a more effective and targeted strategy against malignant growth.

Conclusions

The current investigations present a paradigmatic innovation in the therapeutic intervention of TNBC through the deployment of a dual prodrug nanomedicine construct. This strategically engineered nanoplatform,

encapsulating the potent topoisomerase I inhibitor SN38 and the vaso-occlusive thrombin, is designed to circumvent the intrinsic limitations of traditional chemotherapy. The sequential pH and redox-responsive liberation of prodrugs within the tumor microenvironment ensures a heightened spatiotemporal control over drug release, thereby mitigating systemic toxicities and enhancing the therapeutic index. Our results demonstrate that the nanoplatform, endowed with properties conducive to vasculature occlusion, achieves a significant suppression of tumor growth with minimal systemic toxicity. The uniform distribution and sustained release of SN38, facilitated by thrombin-induced vascular occlusion, underscore the potential of this nanoconstruct to augment the cytotoxic potency of chemotherapy and induce substantial oncocyte demise in TNBC. Moreover, the biocompatibility and pH-responsive release of thrombin from the nanoconstructs further accentuate the precision and safety profiles of this therapeutic intervention.

Prospective researches should concentrate on the optimization of the nanomedicine's physicochemical attributes to augment stability, bioavailability, and targeting fidelity. The exploration of combinatorial therapeutic strategies, synergizing with established treatment modalities, merits investigation to uncover novel paradigms that promise superior patient prognoses. The potential of this nanoplatform to modulate the tumor microenvironment, coupled with its capacity to navigate the complexities of drug resistance mechanisms, positions it as a vanguard in the evolution of cancer therapeutics. Future preclinical and clinical inquiries are essential to discern the long-term safety, efficacy, and pharmacokinetic profiles of this dual prodrug nanomedicine across diverse cohorts of TNBC patients. The transition of these findings into clinical practice could instigate a transformative epoch in the management of TNBC and other malignancies resistant to conventional chemotherapy, offering patients a more efficacious and safer therapeutic alternative.

In summation, the dual prodrug nanomedicine encapsulates a seminal progression in oncology therapeutics, heralding the dawn of a new era of targeted and synergistic cancer therapies. The strategic convergence of nanoscale drug delivery with thrombin-induced angiodeprivation therapy exemplifies the confluence of nanotechnology and oncology, foretelling a revolutionary approach to surmounting the challenges inherent to TNBC.

Supplementary Information

The online version contains supplementary material available at <https://doi.org/10.1186/s12951-025-03302-4>.

Supplementary Material 1

Author contributions

S. L., L.Z., H. C., Y.W. and X.L. designed and performed all the experiments. J. H. and Y. Z. helped with the polymer synthesis. H.C., Y. Z., M. L., W. W. and X.L. helped with the cell experiments. X. L., Y.W., S. Z., K. Z. and Y. Z. assisted with animal experiment. S. L., Y.W. and Q. C. wrote the manuscript. J. H., Y.W. and Y.Z. commented on the manuscript. Q.C. and Y.Z. edited the manuscript and supervised the whole project. All authors reviewed the manuscript.

Funding

This research was funded by National Key Research and Development Program (2022YFD1700200), National Natural Science Foundation of China (32171330), Zhejiang Provincial Natural Science Foundation of China (LZ25H300003), Liaoning Province Science and Technology Plan Joint Program (2024JH2/102600182, 2024JH2/102600184), Zhejiang Provincial Natural Science Foundation of China (LY24H160019), Medical Health Science and Technology Project of Zhejiang Provincial Health Commission (2023RC138), NHC Key Laboratory of Nuclear Technology Medical Transformation (Mianyang Central Hospital, No. 2024HYX022), Liaoning Provincial Key Research and Development Program (2024JH2/102500062), The Clinical Research Fund of Wu Jieping Medical Foundation (320.6750.2020-11-21) and Liaoning Talent Program-Medical Expert Project (YXMJ-LJ-18).

Data availability

No datasets were generated or analysed during the current study.

Declarations

Ethics approval and consent to participate

All animal experimental procedures were performed in accordance with the Guide for the Care and Use of Laboratory Animals as stated by the guidelines of Zhejiang University, Zhejiang Cancer Hospital and China Medical University.

Consent for publication

All authors agree to be published.

Competing interests

The authors declare no competing interests.

Notes

The authors declare the absence of any competing financial interest.

Author details

¹The State Key Laboratory of Molecular Engineering of Polymers, Department of Macromolecular Science, Fudan University, Shanghai 200433, China

²Innovation Center of Yangtze River Delta, Zhejiang University, Jiaxing 314100, China

³Department of Gastric Surgery, Cancer Hospital of Dalian University of Technology, No. 44 Xiaoheyan Road, Dadong District, Shenyang 110042, China

⁴Department of Gastric Surgery, Cancer Hospital of China Medical University, No. 44 Xiaoheyan Road, Dadong District, Shenyang 110042, Liaoning, China

⁵Provincial Key Laboratory of Interdisciplinary Medical Engineering for Gastrointestinal Carcinoma, Liaoning Cancer Hospital & Institute, No. 44 Xiaoheyan Road, Dadong District, Shenyang 110042, China

⁶Department of Clinical Laboratory, Cancer Hospital of Dalian University of Technology, Liaoning Cancer Hospital & Institute, Shenyang 110042, China

⁷Department of Integrated Traditional Chinese and Western Medicine Medical Oncology, Cancer Hospital of China Medical University, Cancer Hospital of Dalian University of Technology, Liaoning Cancer Hospital & Institute, Shenyang 110042, China

⁸Department of Thyroid Surgery, Zhejiang Cancer Hospital, Hangzhou 310022, China

⁹Postgraduate Training Base Alliance of Wenzhou Medical University (Zhejiang Cancer Hospital), Hangzhou 310022, Zhejiang, China

¹⁰Agricultural Genomics Institute at Shenzhen, Chinese Academy of Agricultural Sciences, Shenzhen 518120, China

Published online: 04 April 2025

References

1. Shi Y, Lammers T. Combining nanomedicine and immunotherapy. *Acc Chem Res.* 2019;52(6):1543–54.
2. Cabral H, Kinoh H, Kataoka K. Tumor-Targeted nanomedicine for immunotherapy. *Acc Chem Res.* 2020;53(12):2765–76.
3. Dasgupta A, Sofias AM, Kiessling F, et al. Nanoparticle delivery to tumours: from EPR and ATR mechanisms to clinical impact. *Nat Rev Bioeng.* 2024;2:714–6.
4. Sindhvani S, et al. The entry of nanoparticles into solid tumours. *Nat Mater.* 2020;19:566–75.
5. Nguyen LN, et al. The exit of nanoparticles from solid tumours. *Nat Mater.* 2023;22:1261–72.
6. Nguyen LN, et al. The mechanisms of nanoparticle delivery to solid tumours. *Nat Rev Bioeng.* 2024;2:201–13.
7. Matsumoto Y, et al. Vascular bursts enhance permeability of tumour blood vessels and improve nanoparticle delivery. *Nat Nanotechnol.* 2016;11:533–8.
8. Fang J, Nakamura H, Maeda H. The EPR effect: unique features of tumor blood vessels for drug delivery, factors involved, and limitations and augmentation of the effect. *Adv Drug Delivery Rev.* 2011;63:136–51.
9. Wilhelm S, et al. Analysis of nanoparticle delivery to tumours. *Nat Rev Mater.* 2016;1:16014.
10. Cabral H, Matsumoto Y, Mizuno K, Chen Q, Murakami M, Kimura M, Terada Y, Kano MR, Miyazono K, Uesaka M, et al. Accumulation of sub-100 Nm polymeric micelles in poorly permeable tumours depends on size. *Nat Nanotechnol.* 2011;6:815–23.
11. Gao R, et al. Punctuated copy number evolution and clonal stasis in triple-negative breast cancer. *Nat Genet.* 2016;48:1119–30.
12. Leon-Ferre RA, Goetz MP. Advances in systemic therapies for triple negative breast cancer. *BMJ.* 2023;381:e071674.
13. Li Y, et al. Recent advances in therapeutic strategies for triple-negative breast cancer. *J Hematol Oncol.* 2022;15:121.
14. Zhu S, et al. Recent advances in targeted strategies for triple-negative breast cancer. *J Hematol Oncol.* 2023;16:100.
15. Lee A, Djamgoz MBA. Triple negative breast cancer: emerging therapeutic modalities and novel combination therapies. *Cancer Treat Rev.* 2018;62:110–22.
16. Jain V, et al. A review of nanotechnology-based approaches for breast cancer and triple-negative breast cancer. *J Controlled Release.* 2020;326:628–47.
17. Cai Y, et al. Inhibiting endothelial cell-mediated T lymphocyte apoptosis with integrin-targeting peptide-drug conjugate filaments for chemioimmunotherapy of triple-negative breast cancer. *Adv Mater.* 2023;36:2306676.
18. Ding Y, et al. Chitosan oligosaccharide decorated liposomes combined with TH302 for photodynamic therapy in triple negative breast cancer. *J Nanobiotechnol.* 2021;19:147.
19. Chen Y, et al. A self-assembly nano-prodrug for triple-negative breast cancer combined treatment by ferroptosis therapy and chemotherapy. *Acta Biomater.* 2023;159:275–88.
20. Liu H, et al. Matrix-assisted laser desorption/ionization mass spectrometry imaging (MALDI MSI) for in situ analysis of endogenous small molecules in biological samples. *TRAC Trends Anal Chem.* 2022;157:116809.
21. Zou H, Zhao Z, Wang H, Yang J, Ding J. Construction and assembly kinetics of amino acid–iron nano-assemblies. *Chem J Chin Universities.* 2025;46(1):20240385.
22. Qin C, Yang G, Wei Q, et al. Multidimensional role of amino acid metabolism in immune regulation: from molecular mechanisms to therapeutic strategies. *Chem Res Chin Univ.* 2025;41:1–14.
23. Yang G, Ding J, Chen X. Bioactive poly(amino acids) for multi-modal cancer therapy. *Wiley Interdiscip Rev Nanomed Nanobiotechnol.* 2024;16(4):e1985.
24. Yang G, Liu Y, Chem J, Ding J, Chen X. Self-adaptive nanomaterials for rational drug delivery in cancer. *Acc Mater Res.* 2022;3(12):1232–124.
25. Hao T, Jiang W, Qian L, Yang X, Li W, Zhang B, Li Y, Li Z. Coadministration of Quercetin and indocyanine green via pegylated phospholipid micelles for augmented chem–photothermal combination tumor therapy. *Mol Pharm.* 2024;21(9):4565–75.
26. He Q, Sun C, Liu J, Pan Y. MALDI-MSI analysis of cancer drugs: significance, advances, and applications. *TRAC Trends Anal Chem.* 2021;136:116183.

27. Guo S, Li K, Chen Y, Li B. Unraveling the drug distribution in brain enabled by MALDI MS imaging with laser-assisted chemical transfer. *Acta Pharm Sinica B*. 2022;12:2120–6.

Publisher's note

Springer Nature remains neutral with regard to jurisdictional claims in published maps and institutional affiliations.